Science of the Total Environment 673 (2019) 296–305

Contents lists available at ScienceDirect

Science of the Total Environment

journal homepage: www.elsevier.com/locate/scitotenv

Electro-sorption of ammonium ion onto nickel foam supported highly microporous activated carbon prepared from agricultural residues (dried *Luffa cylindrica*)

Yu-Jen Shih [a,*], Cheng-Di Dong [b], Yao-Hui Huang [c], C.P. Huang [d,*]

[a] Institute of Environmental Engineering, National Sun Yat-sen University, Kaohsiung 804, Taiwan
[b] Department of Marine Environmental Engineering, National Kaohsiung University of Science and Technology, Kaohsiung 811, Taiwan
[c] Department of Chemical Engineering, National Cheng-Kung University, Tainan 701, Taiwan
[d] Department of Civil and Environmental Engineering, University of Delaware, Newark, DE 19716, USA

HIGHLIGHTS

- Differential capacitance of AC was elucidated through pH-dependent voltammetry.
- The adsorption of NH_4^+ was characterized by a multi-layer isotherm.
- Pyrolysis temperature increased the activation energy and heat of electro-sorption.
- Ammonium electrosorption was exothermic and mass transfer limiting.

GRAPHICAL ABSTRACT

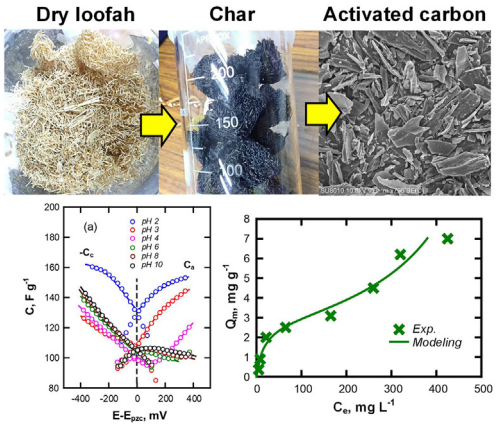

ARTICLE INFO

Article history:
Received 24 January 2019
Received in revised form 2 April 2019
Accepted 4 April 2019
Available online 9 April 2019

Editor: Jay Gan

Keywords:
Biochar
Activated carbon
Multilayer adsorption
Differential capacitance
Polarization
Reversible surface

ABSTRACT

An electrode made of loofah sponge derived activated carbon supported on nickel foam (AC/Ni) was successfully fabricated and used to remove ammonium ion (NH_4^+) from aqueous solution. A multilayer adsorption isotherm was used to describe ammonium electro-sorption on AC/Ni electrodes at different temperature, initial NH_4^+ concentration, and electrical field. The cyclic voltammetry (CV) results suggested that the electrical capacitance of AC/Ni electrodes, with the AC being prepared without preheating (OAC) or with low temperature heating (i.e., 300 AC), were higher than those prepared at high preheating temperature (i.e., 400 AC and 500 AC). Increasing the electro-sorption temperature from 10 to 50 °C decreased the monolayer NH_4^+ adsorption capacity from 5 to ca. 2–3 mg-N g^{-1}, respectively. Background electrolyte, namely, sodium sulfate, exhibited significant competitive effect on the adsorption of ammonium ion at sodium ion concentration > 10^{-2} M. The activation energy and heat of adsorption were 9–23.2 kJ mol^{-1} and −3.7–−10.7 kJ mol^{-1}, respectively, indicating a physisorption and exothermic adsorption characteristics. Based on the kinetics and thermodynamics analysis, there was slight increase in the activation energy with elevating preheating temperature, which increased the quantity of micropores and surface heterogeneity of the AC materials. Overall, results clearly demonstrated that carbon pyrolysis

* Corresponding authors.
E-mail addresses: mcdyessjin@gmail.com (Y.-J. Shih), huang@udel.edu (C.P. Huang).

https://doi.org/10.1016/j.scitotenv.2019.04.066

played a role on the capacitive charging behaviors of electrodes and the efficiency of NH_4^+ electro-sorption on the AC/Ni electrodes.

1. Introduction

Industrial nitrogenous organic compounds are major sources of ammonium (NH_4^+) and nitrate (NO_3^-) in natural waters (Karri et al., 2018; Wells et al., 2018). NH_4^+ is an essential micro-nutrient for eutrophication in lakes, rivers, estuaries, and reservoirs (Stüeken et al., 2016). High level of nitrogen compounds in natural waters can be ecological health hazard (Zhang et al., 2018a). Current methods for the control of ammonium in waters include struvite precipitation, ion exchange, adsorption, filtration, osmosis, and biological treatment. Co-precipitation of ammonium and phosphate driven by the supersaturation of struvite cannot be specific process for ammonium removal (Zeng et al., 2018). Ion exchange resins have relatively low surface area and porosity, while the capacity of electrostatic adsorption is dependent on the cation exchange capacity (CEC) (Park et al., 2011). Adsorption involves the accumulation of solute molecules at an interface, in which, generally, the double-layer capacitance is pH-depending (Huang et al., 2018). The reverse osmosis membrane has severe technical challenges including fouling and high energy cost (Iskander et al., 2018). The well-known Anammox® is effective in treating wastewaters involving the bacterial phylum *Planctomycetes*; whereas biological process needs large land area and long process time compared to chemical methods (Yao et al., 2018). Since NH_4^+ has the lowest nitrogen oxidation state, it can be directly oxidized electrochemically over some active metallic and metal oxide electrodes, such as Pt, NiOOH, and PbO_2 (Ribeiro et al., 2017; Shih et al., 2017, 2018; Kim et al., 2018); or indirectly mineralized by electrochemically produced chlorine from the oxidation of chloride ion over Ti/IrO_2, RuO_2, and boron-doped diamond (BDD) electrodes, which normally have higher oxygen evolution potential than that of chlorine production (Kapałka et al., 2010a, 2010b; Zhang et al., 2018b). However, direct electrochemical oxidation has low nitrogen gas selectivity (Bunce and Bejan, 2011), and indirect chlorination potentially creates toxic chlorinated byproducts (Pérez et al., 2012). Ammonium has a much lower drinking water limit of 0.5 mg-N L^{-1} compared to that of nitrate (50 mg-N L^{-1}) (The Council of the European Union, 1998). Ammonium and nitrate are ubiquitous in surface and groundwater (The Council of the European Union, 2000). Alternative to electrochemical oxidation of ammonium is electro-sorption. The adsorption processes, which normally apply carbon based materials (Moradi, 2016; Mia et al., 2017) and minerals (mainly silicates) (Zhao et al., 2010; Buragohain et al., 2013), as adsorbents of NH_4^+, required long retention time and large space to accommodate the treatment column/reactor, as well as strong acid or base for regeneration of the spent adsorbent. By contrast, electro-sorption has several merits, such as no secondary pollution from spent adsorbent, free of acid/base addition, robustness, and easy regeneration by inversing the electrode polarity (Ahmed and Tewari, 2018). During non-faradaic charging of the double-layer structure at the electrode surfaces, one can recover ions at a potential lower than that of standard redox electro-motive force (EMF) (Oladunni et al., 2018; Zhang et al., 2018c).

Capacitive deionization (CDI) has been suggested as a desalination strategy with respective to conventional ion separation processes such as reverse osmosis and ion-exchange (Porada et al., 2013; Zornitta and Ruotolo, 2018). The specific surface area, pore size and distribution, and electrical double-layer capacitance of the electrode are keys to ion removal efficiency by the CDI process (Ratajczak et al., 2019). Surface modification of electrodes during non-faradaic charging over ideal polarizable electrode (IPE) plays a critical role in ion storage capacity (Ortiz-Bustos et al., 2017). The principle of electro-capillarity states that the differential capacity is minimum at the electrocapillarity maximum (ECM) of the electrode (Anderson et al., 2010; Wu et al., 2016), at which the net electrode surface charge is zero. As the electrode is polarized, the excess charge so formed enhances the adsorption of counter ions within the electrical double layer. Carbon-based materials are ideal for CDI applications mostly due to high specific surface area in addition to the presence of multi-functional groups on the surface, which contribute to extra electrical capacitance resulted from the potential determining ions (pdi) such as proton (H^+) and hydroxide (OH^-) (Hemmatifar et al., 2017). Most hydrous solids, including metal oxides and hydroxides, exhibit intrinsic surface acidity; i.e., the surface acts as a reversible electrode on which the predominance of H^+ and OH^- (potential determining ions) in bulk solution render the surface positively and negatively charged, respectively (Stumm et al., 1970; Huang, 1976; Corapcioglu and Huang, 1987). Until now, the differential capacitance of an electrode-aqueous solution system has not been fully described. According to Stumm et al. (1970) and Huang (1976), the capacitance of a charging surface can be established by change of the concentration (or activity to be exact) of potential determining ions (pdi), i.e., a reversible electrode (Stumm et al., 1970; Huang, 1976; Corapcioglu and Huang, 1987) and the directly applied electrical field (or DC voltage), i.e., a polarizable electrode (Zebardast et al., 2014). Recent studies on capacitive deionization (CDI) tend to focus only on electrode polarization as the major origin of surface charge, which contributes to the capacitance. Furthermore, the performance of CDI system is mostly assessed by the change of conductivity in the system, which provides no information on the adsorption characteristics of both the cations, e.g., Na^+, Ca^{2+}, and the anions, e.g., Cl^- and SO_4^{2-} (Agartan et al., 2019; Bales et al., 2019). The electro-sorption density of specific ions in the presence of an electrical field at specific pH is seldom studied. This work studies the effect of pyrolysis condition on the surface chemistry of hydrous carbon electrodes and its influence on the adsorption characteristics of ammonium ion, in terms of polarizable and reversible electrode charging processes.

Porous carbon materials, including conventional activated carbons (AC) and contemporary nano-textured carbons such as carbon nanotubes (CNTs), nanofibers, aerogels, and graphene (Zornitta et al., 2016) have found applications in the preparation of CDI electrodes. High carbon content and low mineral matter or residues are ideal attributes for the production of ACs; but notably, agricultural byproducts are cheaper than petrochemicals precursors (Yahya et al., 2015; Elmouwahidi et al., 2018). A vegetable sponge (dried loofah) was used to synthesize activated carbon under various pyrolysis conditions as to study the effect of temperature on the electrochemical properties and its effect on the electro-sorption of ammonium ions (NH_4^+). Our preliminary results indicated that the ash content of dried loofah was <1 wt%, lower than that of known agricultural wastes, which will yield higher carbon purity (Ioannidou and Zabaniotou, 2007; Yahya et al., 2015) (Table S1). Note that the dried loofah was not used as a precursor for AC electrodes; rather, it was used to prepare a composite electrode by coating the loofah-derived AC onto nickel foam (AC/Ni). The surface property of AC, as well as the differential capacitance in relation to NH_4^+ sorption capacity, was established. The thermodynamics and kinetics of NH_4^+ removal by AC/Ni electrodes were studied thoroughly as to gain insight into the electrical double layer structure and its effect on the mode and rate of ammonium removal.

2. Materials and methods

2.1. Chemicals

All reagents were of analytical grade and used without purification. Zinc chloride ($ZnCl_2$) was purchased from Sigma-Aldrich Co., USA.

Stock ammonium solution was prepared with ammonium sulfate, $(NH_4)_2SO_4$, (J.T. Baker, USA). Sodium sulfate (Na_2SO_4, Sigma-Aldrich Co., USA) was used as supporting electrolyte. Solution pH was adjusted to specific value with sodium hydroxide (NaOH, Merck KGaA, Germany) and sulfuric acid (H_2SO_4, 95%, Sigma-Aldrich Co., USA). Chemicals used for the analysis of ammonium ion were: (1) sodium hypochlorite (NaClO), (2) sodium phenolate ($NaOC_6H_5{\bullet}3H_2O$), and (3) sodium nitroprusside ($Na_2[Fe(CN)_5NO]$). Sodium phenolate and sodium hypochlorite were purchased from Sigma-Aldrich Co., USA. Sodium nitroprusside was provided by Riedel-deHaën AG, Germany. Deionized water, purified with a laboratory-grade RO-ultrapure water system (resistivity >18.18 MΩ cm), was used to prepared all solutions. The loofah sponge was a dried ripened fruit of *Luffa cylindrica*. The nickel foam (sheet thickness = 2 mm, area density ~250 g/m^2, mesh number = 94 ± 10 openings per linear inch), purchased from Innovation Materials Co., Ltd., Taiwan, was used as the porous substrate to immobilize the AC samples.

2.2. Experimental procedure

To synthesize the activated carbon (AC), a fibrous cushion of loofah sponge was cut into pieces of 2 cm × 2 cm in size. Before activation, the biochar was obtained first by heating (i.e. carbonization at a rate of 5 °C/min) the dried raw loofah under N_2 atmosphere at 300, 400, and 500 °C, respectively for 2 h. The biochar products, designated as 300C, 400C, and 500C, individually, were ground to <100 mesh (74 μm) before further treatment. To activate the carbon, raw original loofah and biochar 300C, 400C and 500C were thoroughly mixed with $ZnCl_2$ at a mass ratio of 4:1 ($ZnCl_2$ to C). The mixture became sticky after drying at 110 °C to remove the water solvent and was then transferred to a tubular furnace to start the pyrolysis under N_2 atmosphere at 800 °C (heating rate = 5 °C/min, 2 h). The resulted AC samples were denoted as OAC, 300 AC, 400 AC, and 500 AC, respectively. (Note that OAC was prepared directly from dried raw loofah without preheating to biochar.) To remove the residual activating agent, i.e. $ZnCl_2$, AC samples were washed in 0.5 M HCl then deionized water several times until the pH of the rinse reached around 7.

The AC slurry was prepared by mixing a given amount of AC with poly(vinylidene fluoride) (PVDF) as binder (~5 wt%), N-Methyl-2-pyrrolidone (NMP) (Sigma-Aldrich Co., USA) as solvent, and then the mixture was uniformly spread onto the nickel foam with a painter brush (Fig. 1a), denoted as AC/Ni. Prior to all experiments, the AC/Ni electrode was soaked in 0.5 M NaOH overnight to increase the hydrophilicity. A Ti/IrO_2 cylinder, 5 cm in diameter with a working geometric area of ~80 cm^2, was positioned at an average electrode-to-electrode distance of 0.5 cm and used as the counter electrode. Electrochemical experiments were carried out using a potentostat (CHI611C, CH Instruments, Inc., USA) equipped with a reference electrode of Hg/HgO/1 M NaOH (E^0 = 0.14 V vs. NHE) (RE-61AP, ALS Co. Ltd., JAPAN).

The differential capacitance of the electrode, C (F), was calculated from the voltammetry measurements according to the following equation:

$$C \equiv \frac{d\sigma}{dE} = \frac{Idt}{dE} = \frac{I}{v} \tag{1}$$

where σ is the surface charge density (C m^{-2}) and E is the polarizable potential (V). By definition, charge is the product of current (I, A) and time (t, *sec*), and v = dE/dt is the voltage scan rate (V s^{-1}). For inert 1:1 electrolyte, the capacitance from positive (C_c) and negative (C_a) sweeps were ideally symmetric, that is, C_c will be equal but opposite in sign to C_a at EMC (E_{pzc}), namely,

$$\begin{aligned} C_a &= \frac{d\sigma_+}{dE} \\ C_c &= \frac{d\sigma_-}{dE} \\ at\ E &= E_{pzc}, C_a = -C_c \end{aligned} \tag{2}$$

where σ_+ and σ_- are the surface excess (or charge) due to the accumulation of the positively and the negatively charged species, respectively. For a reversible surface, the surface potential, Ψ_o, is related to pH according to the Nernst equation (Stumm et al., 1970; Huang, 1976), i.e.,

$$\Psi_0 = -\frac{2.303RT}{nF}\left(pH - pH_{pzc}\right) = -0.05915 \times \left(pH - pH_{pzc}\right) \times (@T = 20^{\circ}C) \tag{3}$$

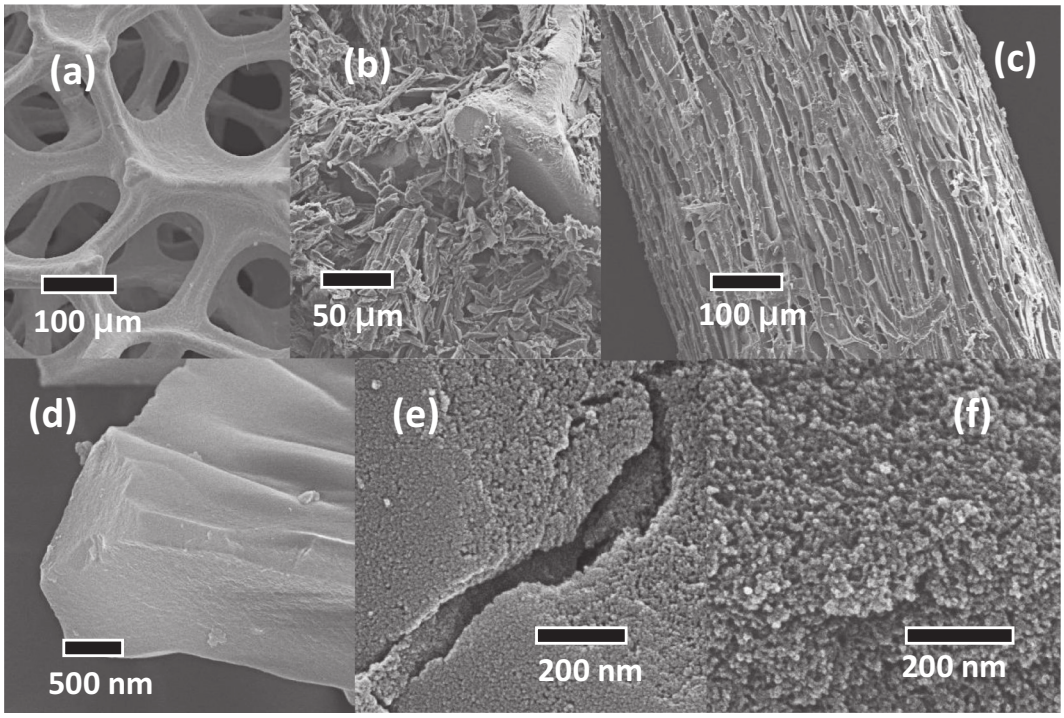

Fig. 1. SEM observation of (a) Ni foam, (b) OAC/Ni electrode, (c) the loofah sponge, and (d) biochar heated under 500 °C (500C), (e) OAC, (f) 500 AC.

where R (8.314 J mol^{-1} K^{-1}) is the gas law constant and T is the absolute temperature (K). The differential capacitance of a reversible electrode, C_{pH}, is:

$$C_{pH} = \frac{d\sigma_0^{pH}}{d\Psi_0} = \frac{d\sigma_0^{pH}}{dpH}\frac{dpH}{d\Psi_0} = -16.9\frac{d\sigma_0^{pH}}{dpH} \quad (4)$$

The observed total capacitance, C, is resulted from two capacitors in parallel, one of reversible (C_{pH}) and the other of polarizable (C_E). At pH_{pzc} (σ_0^{pH} is zero) and E_{pzc}, (or electrocapillarity maximum, ECM) the differential capacitance, C, is at its minimum; so are C_E and C_{pH}. With reference to Eq. (4), the total differential capacitance is: (Supporting data).

$$C = \frac{d\sigma_0}{dE} = \frac{d\sigma_0^E}{dE} + \frac{d\sigma_0^{pH}}{dE} = \frac{d\sigma_0^E}{dE} - 16.9\frac{d\sigma_0^{pH}}{dpH} = C_E + C_{pH} \quad (5)$$

The main idea of integration of capacitances from a polarizable and reversible surface is depicted in Fig. S1.

Cyclic voltammetry experiments were conducted by scanning the potential at specific pH value, starting initially from 0 and in the range of −0.4 V to +0.6 V, where no faradic reduction occurred. The current profile was taken after the 4th to 5th runs of CV scanning, when signals became reproducible (Fig. S2).

Batch ammonium electro-sorption experiments were conducted at an initial ammonium concentration of 50 mg-N L^{-1} (or 3.57×10^{-3} M) at −1.0 V (vs. Hg/HgO) for 80 min and then turning the working potential to +0.1 V for 40 min for desorption, both at temperature of 10–50 °C. Note that the initial pH of the $(NH_4)_2SO_4$ solution, in the range of 20–500 mg-N L^{-1} (or 3.5×10^{-3}–3.57×10^{-2} M) was ca. 6.12–5.42, which remained relatively constant throughout the entire ammonium electro-sorption run. That is, loss of ammonium nitrogen through ammonia volatilization was highly unlikely.

2.3. Chemical analyses

A flow injection analyzer (FIA, Lachat's Quik Chem 8500 Series 2, USA) based on the Berthelot reaction was used to analyze the concentration of aqueous NH_4^+. The indophenol method (at 630 nm) was a catalytic reaction among phenolate, hypochlorite, and ammonia, with nitroprusside as the catalyst; the detection limit was 0.2 μg L^{-1} for NH_4^+-N.

2.4. Surface characterization

A scanning electron microscopy (SEM, JSM-6700F, JEOL Ltd., Japan) was used to characterize the micro-morphology of the electrodes. X-ray photoelectron spectroscopy (XPS, PHI 5000 VersaProbe, Physical Electronics, Inc., USA) with a monochromatic Al Kα X-ray source (1487 eV) was used to characterize the chemical state of AC. A zetasizer (Malvern Nano ZS MRK 791-02, UK) was used to determine the surface potential of AC as a function of pH.

3. Results and discussion

3.1. Property of activated carbon

The nickel substrate is a metallic foam with 3D open pores mainly of pentagonal shape and 250 μm in size, which is well intercalated with AC particles (Fig. 1a and b). The carbonized char of dried loofah sponge has a fiber texture of ~100 μm in diameter (Fig. 1c). In order to ensure workability of carbon slurry (which was made of char/AC, PVDF, and solvent NMP) in uniformly filling the pores of the nickel substrate, the pyrolyzed AC was finely ground and sieved to under 100 μm before being incorporated onto the Ni foam. After activation with $ZnCl_2$, a large number of macro-size cavities were created over the smooth surface of carbonized char (500C, Fig. 1d); whereas increasing the carbonization temperature decreased the size of micropores as indicated by the morphological change between OAC (Fig. 1e) and 500AC (Fig. 1f).

Fig. 2 presents the XPS spectra of pyrolyzed char and activated carbon in terms of C 1 s and O 1 s atomic orbitals. Table 1 lists the corresponding band position and the percentage of surface functional groups. A general carbon based material has C 1 s peak deconvoluted into four peaks representing aromatic C—C/C—H (284.81–285.03 eV, C1), aromatic C—O (286.42–286.73 eV, C2), ketone C═O (287.81–288.03 eV, C3) and carboxylic COO (288.60–289.55 eV, C4) (Singh et al., 2014). For carbonized loofah samples, aromatic compounds were the major C groups, which were similar to that of carbon black (Cheng et al., 2006). Meanwhile, the intensified signal of aromatic ring with increasing carbonization temperature suggested that the precursor, treated at high temperature (as biochar) to form into AC, pronounced crystallized graphitic structure after activation. In the O 1 s region, the peaks were corresponding to binding energy of 533.2, 531.5, 529.8, 532.4, and 534.5 eV for carbonyl groups in ether (O1), amides and anhydrides (O2), hydroxyl oxygen (O3), esters (O4), and chemisorbed water (O5), respectively (Chiang et al., 2011). Compared to carbonized char (300C—500C), the appearance of C═O (C3) and COO (C4) groups of C 1 s bands after activation (OAC-500AC, Table 1) was mainly contributed to the formation of oxygen-containing aromatic functionalities. Further, the increase in O═C (O2) and O═C—O (O4) bands is evident of the presence of quinone and carboxyl groups, respectively, which implied oxidized AC surface upon increasing activation temperature. Also, the reversible transition of quinone-hydroquinone ($Q + 2e^- + 2H^+ = QH_2$) has been suggested to give rise of the pseudo-capacitance during the charging/discharging cycle (Golub et al., 1987). In other words, AC prepared at higher temperature exhibited greater charging current, possibly originated from the faradaic reaction of Q/QH_2 redox (Pandi et al., 2016). Furthermore, for AC prepared under higher temperature a greater portion of charging current may originate from the faradaic reaction of Q/QH_2 redox (Pandi et al., 2016).

3.2. Electrochemical analysis of AC/Ni electrodes

Cyclic voltammetry (CV) was used to assess the electrochemical behavior of the Ni foam-based carbon electrodes within the potential window of −0.4 and + 0.6 V (pH 2–10, 0.1 M Na_2SO_4) as shown in Fig. 3. The symmetrical voltage-current profile, with respect to voltage sweeping in the anodic and cathodic direction, was brought by the capacitive charging of sulfate and sodium ions, respectively. In other words, the magnitude of current response from the non-faradaic charging was dependent on the capacitance of the electrode. Compared to AC (Fig. 3a and b), the carbonized char of loofah (500C/Ni, Fig. 3c) had a much lower capacitive current. Note that faradaic peaks appeared only for carbonized samples, i.e. biochar, at low pH. A reversible couple such as carboxylic or hydroquinone groups might emerge on the biochar surface at acidic pH. Redox reaction occurred on the surface functional groups could give rise to the pseudocapacitance of the carbon electrode. Chen et al. (2013) and Xu et al. (2015) also reported that under acidic condition, the functional groups, such as carboxylic or quinone, were responsible for the pseudocapacitance, which became pronounced on the carbon surface without the interference of electrical-double-layer charging current.

According to Eq. (1), the differential capacitance can be obtained by plotting the anodic (I_a) and cathodic (I_c) current versus scan rate (note that the current was extracted from Fig. 3) at given E. As mentioned above, the surface charge of a metal oxide/AC electrode in aqueous solution has two origins: (a) changing the electrode potential (polarization), and (2) changing the pH of the aqueous solution, i.e., reversible hydrous surface (Stumm et al., 1970; Huang, 1976; McCafferty, 2010). The isoelectric point or point of zero charge (pH_{pzc}) is the pH at which the sum of surface proton excess is equal to that of the surface proton

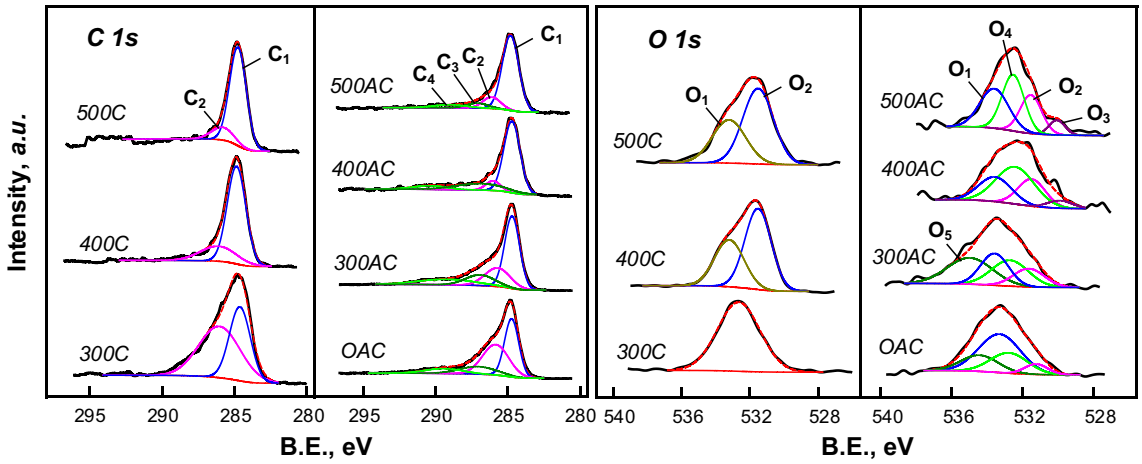

Fig. 2. XPS analysis of pyrolyzed biochar (300C, 400C, 500C), and activated carbon (OAC, 300 AC, 400 AC, 500 AC) in terms of C 1 s and O 1 s (C 1 s contains groups of C—C/C—H (C1), aromatic C—O (C2), ketone C═O (C3) and carboxylic COO (C4), respectively; O 1 s present as oxygen in carbonyl groups of ether (O1), amides and anhydrides (O2), hydroxyl oxygen (O3), esters (O4), and chemisorbed water (O5), respectively).

deficient. The potential of zero charge (E_{pzc}) is the electrocapillary maximum at which the surface excess of cations is equal to that of the anions (Stumm et al., 1970; Huang, 1976). Fig.S3 shows the zeta-potential of biochar and AC samples as a function of pH in the presence of KCl at concentration 10^{-3}–10^{-1} M. Result showed a pH_{pzc} of around pH 2–3 for 500 AC (Fig. S3a). The low pH_{pzc} is indicative of abundant oxygen-containing groups on biochar and AC surfaces as revealed by XPS analysis (a typical L-type AC, Yahya et al., 2015). Carbonization (500C) and activation without and with preheating (OAC and 500AC) did not alter the zeta potential as a function of pH (Fig. S3b).

The C_a and -C_c value were obtained from the C-V curve at various pH values (exemplified by OAC/Ni electrode in Fig. 4a which shows the differential capacity as a function of applied voltage at different pH values). It is clear that the minimum differential capacitance, C_{pzc}, occurred at E_{pzc}. Table S2 lists the minimum differential capacitance as a function of pH. The C_{pzc} for charging in 0.1 M Na_2SO_4 electrolyte, followed the order 300 AC (118–133 F g^{-1}) > OAC (102–128 F g^{-1}) > 400 AC (78–91F g^{-1}) > 500 AC (70–85 F g^{-1}) ≫ 500C (3.7–4.0 F g^{-1}). Fig. 4b is a plot of the minimum differential capacitance, C_{pzc}, as a function of pH for all carbon electrodes studied, indicated that the pH_{pzc} was around 4.0; whereas the pH_{pzc} of biochar (500C) and activated carbon (OAC and 500AC) were in the range of 2–3 from zeta-potential measurements in the absence externally applied voltage (Fig. S3). Intuitively an externally applied voltage will alter the pH_{pzc} of the electrode. Shih et al. (2015, 2017) reported minimum C_{zpc} at pH_{pzc} 5 and 9 for the Pt/graphite and the PbO_2 electrodes, respectively. Since results of zeta-potential measurements indicated that the carbon surface was negatively charged over a wide pH range, the C_{pzc} value remained relatively constant.

Table 1
XPS analysis of biochars and ACs/Ni electrodes.

Band	C 1 s			
	C1	C2	C3	C4
eV	284.5	286.3	287.5	289
Samples	C—C, C—H	C—O	C═O	COO
300C (%)	42	57	–	–
400C (%)	76	23	–	–
500C (%)	85	14	–	–
OAC (%)	39	38	13	8
300AC (%)	49	21	14	14
400AC (%)	67	8	18	7
500AC (%)	75	12	6	6

Band	O 1 s				
	O1	O2	O3	O4	O5
eV	533.2	531.5	529.8	532.4	534.5
Samples	O—C	O═C	—OH	O═C—O	H_2O
300C (%)	100	–	–	–	–
400C (%)	39	60	–	–	–
500C (%)	38	61	–	–	–
OAC (%)	49	7	–	23	18
300AC (%)	24	16	–	26	33
400AC (%)	25	23	5	45	–
500AC (%)	33	24	6	36	–

3.3. Batch electro-sorption of ammonium ions

Fig. 5a shows the effect of supporting electrolyte (Na_2SO_4) on NH_4^+ removal by the 500AC/Ni electrode as a function of time. Results show that NH_4^+ concentration decreased continuously during electrode charging at −1.0 V (vs. Hg/HgO) and approached the steady state condition in 80 min. High percentage of NH_4^+ uptake onto OAC/Ni was released to the solution when reversing the potential to +0.1 V (vs. Hg/HgO). The extent of desorption reached >90% quickly in 40 min. The adsorption/desorption profile at an initial ammonium concentration of 50 mg-N L^{-1} (~3.5 mM) suggested an obvious competitive charging between NH_4^+ and Na^+ when Na_2SO_4 concentration was up to 10^{-2} M (Fig. 5a).

In order to establish the electro-ammonium adsorption isotherms, a series of adsorption experiments were run at different initial NH_4^+ concentrations, e.g., 20–500 mg-N L^{-1} (Fig. 5b). The adsorption capacity as a function of equilibrium ammonium concentration was analyzed with various models, including monolayer Langmuir, multilayered Langmuir, and the Fruendlich adsorption isotherms (Fig. S4 and Table S3). Results showed either the monolayer or the multilayer Langmuir adsorption isotherms fitted the adsorption data better than that of the Fruendlich as evidenced of larger R^2 value (Table S3). It is no surprising that multi-layer adsorption will play a role in ammonium adsorption considering the heterogeneity nature of the biochar surface (Sing et al., 1985; Chakraborty and Sun, 2014; Muttakin et al., 2018). The type II adsorption curve better describes NH_4^+ adsorption than that of type I as the concentration of supporting electrolyte (Na_2SO_4) increases. (Note: According to IUPAC, adsorption isotherm has four major classifications including type I, [Monolayer Langmuir], type II [multilayer Langmuir], type III [high affinity], and type IV [capillary condensation] classes (Sing et al., 1985; Chakraborty and Sun, 2014; Muttakin et al., 2018)).

Furthermore, electrical charging of the carbon surface can create sites of different adsorption energy. Since electro-sorption is typically diffusion-controlled (Garland et al., 2002), NH_4^+ fills up the external surface and meso-pore first, and then penetrates deeper into micro-pore at

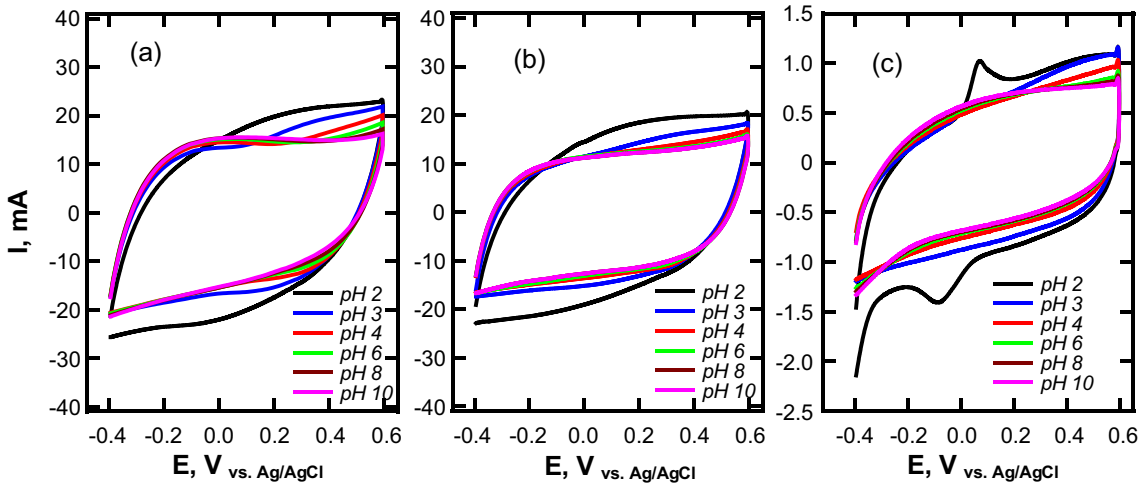

Fig. 3. CV curve at different pH. (a) 500AC/Ni; (b) OAC/Ni; (c) 500C/Ni. Experimental conditions: supporting electrolyte = 10^{-1} M Na_2SO_4; scan rate = 2 mV s^{-1}; effective mass of carbon = 0.073 g for 500 AC, 0.067 g for 500C and OAC.

higher concentrations. Considering a multilayer adsorption, the coverage of total adsorbate (θ) in subsequent layers should be (Wang et al., 1998):

$$\theta = \frac{K_1 C_e}{(1-K_2 C_e)[1+(K_1-K_2)C_e]} \tag{6a}$$

or in terms of adsorption capacity, Q_e,

$$Q_e = \frac{K_1 C_e Q_1}{(1-K_2 C_e)[1+(K_1-K_2)C_e]} \tag{6b}$$

where C_e = equilibrium NH_4^+-N concentration (mg L^{-1}), Q_e = equilibrium NH_4^+ adsorption density (mg-N g^{-1}), K_1 = equilibrium constant for the first layer adsorption (L mg^{-1}), K_2 = equilibrium constant for multilayer adsorption (L mg^{-1}), and Q_1 = surface site density of monolayer adsorption (mg-N g^{-1}) for NH_4^+-N. When the first layer adsorption is more predominated, i.e. K_2 being negligible and Eq. (6a) and (6b) resumes the conventional (monolayer) Langmuir equation (i.e., $K_1 = K_L$ and $Q_1 = Q_m$, monolayer capacity). Table S3 summarizes the parameters obtained from fitting the Q_e versus C_e data (Fig. 5b) according to Eq. (6a) and (6b). Both K_1 and K_2 increased with increasing Na_2SO_4 concentration; whereas the monolayer capacity (Q_1) decreased significantly (from 4.5 mg-N g^{-1} to 0.83 mg-N g^{-1} when Na_2SO_4 concentration increased from 10^{-3} M to 10^{-1} M Na_2SO_4). Results showed that the electrical double layer was compressed at high supporting electrolyte concentration as expected, which facilitated NH_4^+ and Na^+ adsorption onto the negatively charged AC electrode, hereby increased the adsorption constant (or energy) (Sun et al., 2018). However, Na^+ competition decreased NH_4^+ adsorption capacity. In a CDI system, the valence and hydrated radii of ions determine not only the removal efficiency (selectivity), but also the electrical double layer structure (specifically, the thickness of diffuse layer), the specific chemical adsorption of ions (surface complexation), and the capacity for different potential-determining species (Choi et al., 2019). In addition to the effect of supporting electrolyte concentration on the removal of NH_4^+, because electro-sorption is performed with a potential drop between the pair of electrodes, the selectivity of NH_4^+ shall be thoroughly studied to gain insight into the effect of co-ions and the molar ratio of anion to cation species in future investigation.

Adsorption/desorption experiments were investigated at different temperature to demonstrate the kinetics of NH_4^+ electro-sorption. As

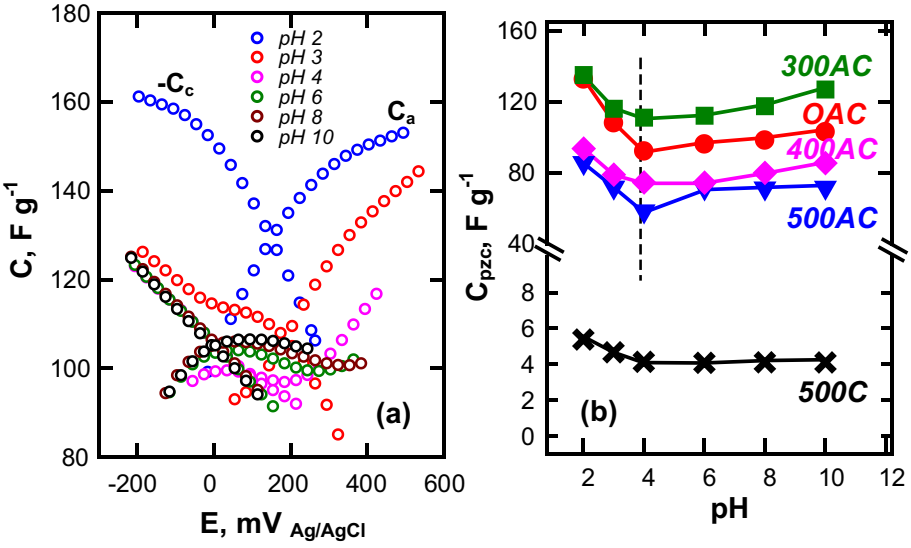

Fig. 4. (a) Effect of pH on electrical capacitance of OAC/Ni electrode as a function of electrode potential; (b) electrical capacitances (at E_{pzc}) of ACs/Ni electrodes as a function of pH (10^{-1} M Na_2SO_4).

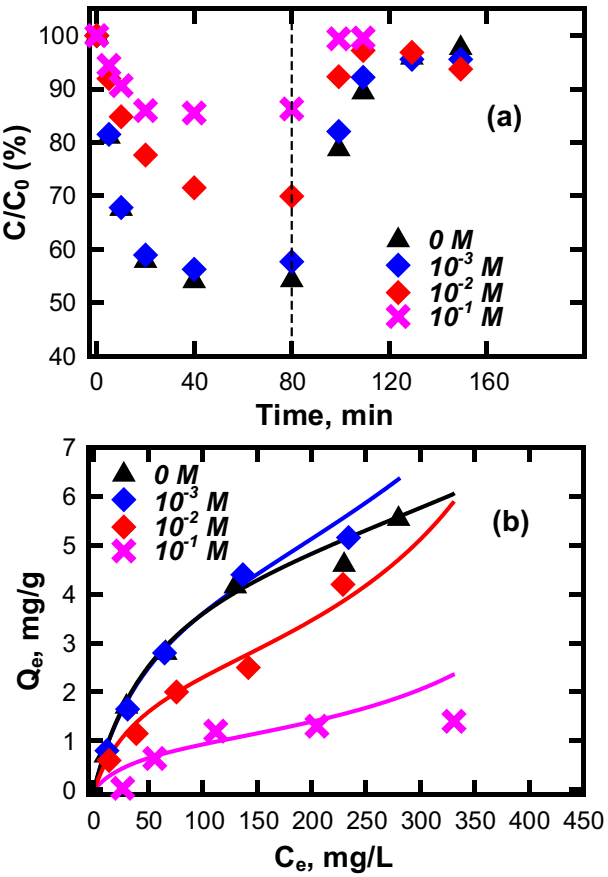

Fig. 5. Effect of supporting electrolyte concentration on NH_4^+ removal. (a) Percent remaining at initial NH_4^+-*N* = 50 mg L^{-1}; (b) adsorption isotherm. Experimental conditions: [Na_2SO_4] = 0–10^{-1} M; working potential = −1.0 V (vs. Hg/HgO) for adsorption and + 0.1 V (vs. Hg/HgO) for desorption; initial NH_4^+-*N* = 20–500 mg L^{-1}.

shown in Fig. S5, the NH_4^+ adsorption capacity as a function of time over four Ni foam-based electrodes: OAC, 300 AC, 400 AC, and 500 AC. NH_4^+ adsorption capacity (mg-N g^{-1}) increased at −1.0 V (vs. Hg/HgO) in 80 min, and at least >80% NH_4^+ adsorbed on the electrode was desorbed to the solution by reversing the polarity to +0.1 V (vs. Hg/HgO) in 40 min. Both electro-sorption and desorption were modeled according to the following general rate law (Eq. (7)),

$$\frac{dQ_t}{dt} = k_1(Q_e - Q_t)^n \tag{7}$$

where Q_t and C_t denote the adsorption capacity (mg-N g^{-1}) and concentration (mg L^{-1}) of NH_4^+-N at time t, respectively. The adsorption capacity was calculated by the following equation:

$$Q_t = \frac{(C_0 - C_t) \times V}{m} \tag{8}$$

where V is reaction volume (L) and *m* is mass of AC on the Ni foam support (g). Results of preliminary runs showed high degree of reproducibility (Fig. S6). Unless otherwise mentioned, all ammonium sorption data were averages of triplicate. For n = 1, the adsorption kinetics follows the pseudo-first-order rate expression, which has been generally applied in the study of adsorption and CDI processes (Gaikwad and Balomajumder, 2017; Bharath et al., 2017; Li et al., 2018; Zornitta and Ruotolo, 2018), and the capacity profile is a time function, i.e.,

$$Q_t = Q_e\left(1 - e^{-k_1 t}\right) \tag{9}$$

For desorption:

$$Q_t = Q_e + (Q_{e,des} - Q_e)e^{-k_{1,des}t} \tag{10}$$

where k_1 and $k_{1,des}$ are the adsorption and desorption rate constants, respectively; $Q_{e,des}$ is the equilibrium capacity of NH_4^+ at desorption. The rate constants derived from fitting electro-sorption date with Eq. (9) and Eq. (10) are shown in Fig. 6a and b, respectively. A linear regression of ln k versus 1/T generates the slope ($-E_a/R$) and intercept (lnA), from which the activation energy, E_a (J mol^{-1}) (gas constant R = 8.314 J K^{-1} mol^{-1}) and the collision frequency, A (min^{-1}), respectively, can be calculated according to the Arrhenius equation:

$$\ln k_1 = \ln A - \frac{E_a}{R}\left(\frac{1}{T}\right) \tag{11}$$

Results showed that the sorption/desorption rate was higher at higher temperature due to the mass transfer-limiting nature of the ammonium electro-sorption process. The diffusion coefficient of ions increases with increase in temperature (Sharma et al., 2013). The magnitude of activation energy determines the rate-limiting step of adsorption as physical (or mass transport) or surface (or chemical) reaction. High activation energy implies temperature-sensitive reaction (Sandeep et al., 2017; Mowla et al., 2019). If the activation energy is relatively low, e.g., between 5 and 40 kJ mol^{-1}, mass transport step would control the adsorption process. An increase in E_a value with increasing preheating temperature (as shown in Fig. 6c) implies that the mechanism of NH_4^+ sorption among all AC electrodes, E_a being in the range of 9 to 23.2 kJ mol^{-1} for adsorption and 10.8 to 19.8 kJ mol^{-1} for desorption, belonged to physisorption and mass transport controlled reaction. (Collision frequencies *A* are provided in Table S4.) Our results were close to that of NaCl removal using typical desalination system reported in the literature. For example, Mossad and Zou (2013) and Wimalasiri et al. (2015) reported an activation energy of 6.67 and 12.36 kJ mol^{-1} on AC and graphene electrode, respectively. For a capacitive deionization process, the rate of ion capture was strongly dependent on the effective diffusion of counter ions toward the charged porous structures. The low activation energy might be attributed to the greater mesoporosity that resulted in higher capacitance for OAC and 300 AC according to C-V results (Fig. 4). (Note: The BET specific surface area of OAC and 300AC were around 1500 m^2 g^{-1} versus < 1000 m^2 g^{-1} of 500AC.) Moreover, at the initial NH_4^+-N concentration of 50 mg L^{-1}, the adsorption capacity (Q_e) decreased with increase in temperature for all electrodes, which suggested that the carbon surface became less accessible to NH_4^+ for sorption at higher temperature (Fig. 6d). Temperature can influence the sorption capacity of a carbon electrode through its electrical double layer structure. The diffuse layer thickness (Debye length, κ^{-1}), according to the Debye-Huckel approximation is: $\kappa^{-1} = \sqrt{(\varepsilon_w k_B T)/(\Sigma n_i^0 z_i e^2)}$, in which n is number of ion per unit volume, z is charge, ε_w is relative dielectric constant of water, k_B is Boltzmann constant, and T is temperature (AlMarzooqi et al., 2014). Increase in T increases the thickness of diffuse layer (κ^{-1}), which in turn decreases differential capacitance according to the following temperature dependent integral capacitance:

$$C_{int} = -\sigma_d/\psi_d = \kappa\varepsilon \tag{12}$$

Fig. S7 shows the effect of temperature on electro-sorption isotherms of NH_4^+ over four electrodes tested. It appeared that higher temperature exhibited multilayer adsorption isotherms. Fig. S8 shows K_1 and K_2 as a function of temperature fitted the adsorption data with multilayer Langmuir adsorption model (Eq. (6a) and (6b)). Results showed an increase in K_2 with increasing temperature for all electrodes, indicating multi-layer adsorption. As temperature decreased, adsorption became monolayer type (i.e., Eq. (6a) and (6b) became a monolayer Langmuir adsorption isotherm) and K_2 became relatively insignificant with respect to K_1. In other words, the accumulation of ammonium

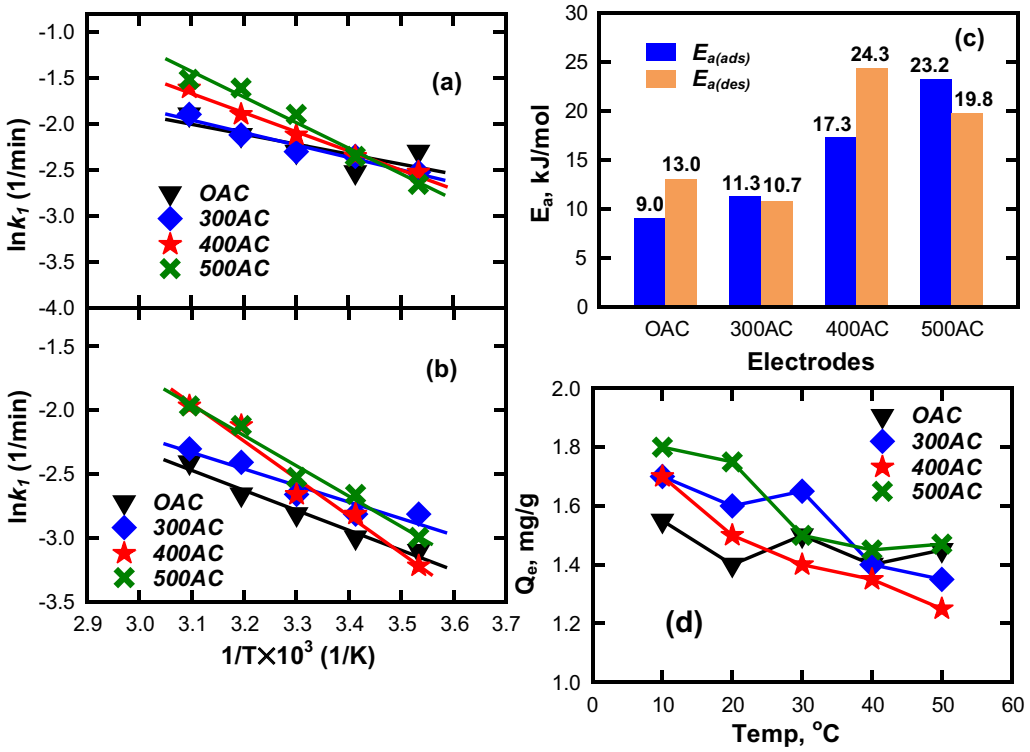

Fig. 6. Arrhenius plots of (a) electro-sorption (−1.0 V vs. Hg/HgO); (b) desorption (+0.1 V vs. Hg/HgO) of NH_4^+; (c) kinetic parameter of NH_4^+ electrochemical adsorption and desorption; (d) equilibrium capacity of electro-sorption as a function of temperature over ACs/Ni electrodes.

became multilayer as temperature elevated. This has prompted the hypothesis that the second layer accumulation is resulted from surface heterogeneity in equilibrium with high concentration of NH_4^+. That is, the difference in charging rate between meso- and micro-pores becomes significant with elevating temperature. The monolayer capacity, Q_m (according to the multilayer adsorption model, Eq. (6a) and (6b)) was adversely proportional to temperature (Fig. 7a). From 10 to 50 °C, the monolayer NH_4^+ adsorption capacity decreased from 5 to ca. 2–3 mg-N g^{-1}. The adsorption of NH_4^+ on carbon-based materials was exothermic, that is, increase in temperature did promote adsorption.

Generally, since K_1 is one-order of magnitude larger than K_2, therefore, the Gibbs free energy of adsorption (ΔG^0) for the first layer (monolayer) only was calculated.

$$\Delta G^0 = -RT\ \ln K_1 \tag{13a}$$

and

$$-\frac{\Delta G^0}{RT} = \ln K_1 = -\frac{\Delta H_{ads}}{RT} + \frac{\Delta S_{ads}}{R} \tag{13b}$$

According to the van't Hoff equation, the Gibbs free energy change is a function of the enthalpy (ΔH_{ads}) and entropy change (ΔS_{ads}) of adsorption (Saffarionpour et al., 2019), i.e.,

$$\frac{\partial\ \ln K_1}{\partial(1/T)} = -\frac{\Delta H_{ads}}{R} \tag{14}$$

The thermodynamic parameter, ΔH_{ads}, can be calculated from the slope and intercept of the van't Hoff plot ($\ln K_1$ versus 1/T, Fig. 7b). The ΔH_{ads} of ammonium adsorption slightly increased with increasing preheating temperature, but was <20 kJ mol^{-1} for all AC/Ni electrodes as shown in Fig. 7c.The typical ΔH^0_{ads} for physio-sorption was in the range of 2.1–20.9 kJ mol^{-1}, and that of chemisorption was between 80 and 200 kJ mol^{-1} (Liu and Liu, 2008; Agarry et al., 2015). According to the results of voltammetry study, the differential capacitance may decrease at higher pyrolysis temperature because of decrease in specific surface area. Results again clearly indicated the physical nature of ammonium adsorption, i.e. maximum capacity, did not substantially differ among OAC and ACs; whereas the activation energy and heat of adsorption increased. Overall, from the point view of kinetics and thermodynamics, low activation energy and heat of adsorption favor fast removal of ammonium ions and subsequent electrode regeneration in a CDI system. Since the chemical bonding between NH_4^+ and AC electrode was weak, the cationic ammonium was able to adsorb and desorb readily under low electric field (thus low electricity energy) in cathodic and anodic mode of polarizability, respectively.

4. Conclusion

We have successfully synthesized several carbon materials form an agricultural byproduct of dried loofah sponge, with and without activation under different temperature in nitrogen gas. The carbon materials were supported on metallic Ni foam to prepare electrodes for studying the capacitive properties during the electrosorption of ammonium in dilute aqueous solutions. Cyclic voltammetry was used to analyze the electrochemical properties of the AC/Ni electrodes in terms of electrical double layer which charging mechanisms was derived from polarization (electrocapillarity) and reversible potential determining ions, namely H^+ and OH^-. The reversible hydrous carbon surface in addition to electrode polarization, together, contributed to the total differential capacitance of the electrode-electrolyte systems. The minimal differential capacitance of AC/Ni, C_{pzc}, varied slightly with pH and was around pH 4, which was close to the pH_{pzc} (=2–3). Since the AC surface was negatively charged over a wide pH range, the electrical capacitance was not pH-dependent and remained relatively constant with respect to pH. Results showed that without preheating or with low temperature (300 °C) heating, the AC/Ni electrode exhibited greater differential capacitance than that heated at higher temperature (400 °C and 500 °C). Nevertheless, results of batch NH_4^+ adsorption did not show significant

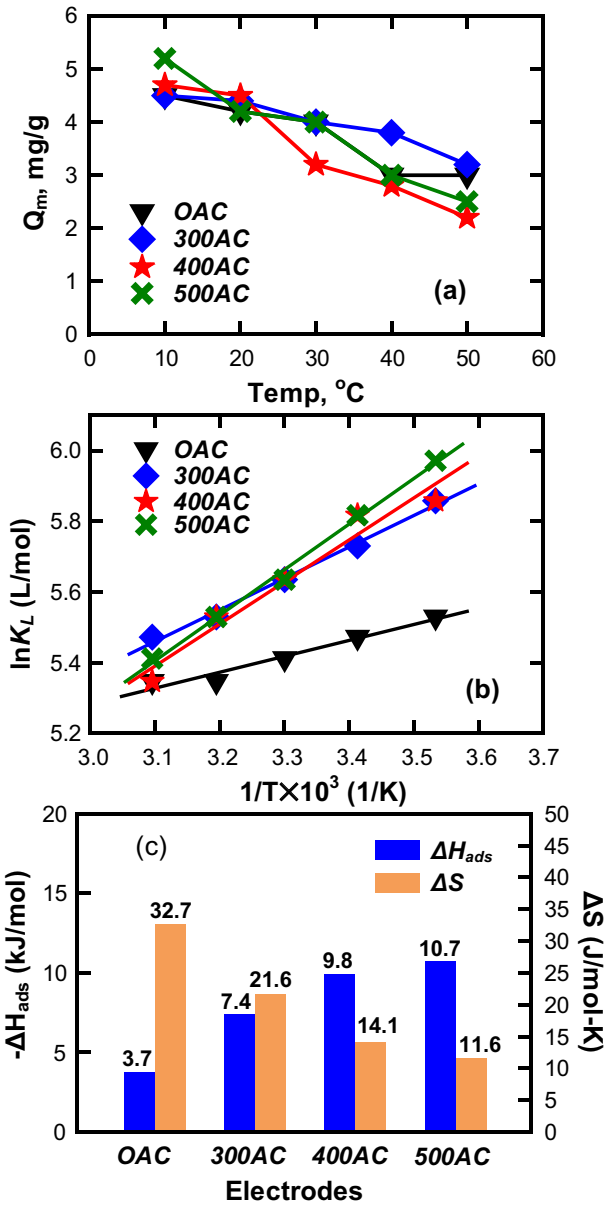

Fig. 7. (a) Maximum capacity for NH_4^+ as a function of temperature; (b) van't Hoff plot of $\ln K_L$ versus *1/T*. (c) Thermodynamic parameter of NH_4^+ electro-sorption on AC/Ni electrodes.

difference among AC materials studied. The activation energy and heat of NH_4^+ adsorption decreased with increasing pyrolytic temperature. The activation energy (E_a = 9–23.2 kJ mol^{-1}) and heat of adsorption ($-\Delta H_{ads}$ = 3.7–10.7 kJ mol^{-1}) of AC, nonetheless, were low, which enabled fast adsorption/desorption. Electro-sorption of NH_4^+, has several merits over conventional AC adsorption process. Electro-ammonium, operated under low gas evolution overpotential, is of low cost and free of strong acid/base chemicals use during the desorption/regeneration cycle in conventional adsorption, and has relatively short process time. Overall, electro-sorption is a promising alternative to conventional carbon adsorption processes.

Acknowledgements

This work was supported by The Ministry of Science and Technology, Taiwan, under Contract No. 104-2218-E-006 -020 -MY3. National Sun Yat-sen University and National Kaohsiung University of Science and Technology, Taiwan provided additional supports, under contract number NKUSTNSYSU 107-P07. US NSF IOA (1632899) provided additional support to CPH.

Appendix A. Supplementary data

Supplementary data to this article can be found online at https://doi.org/10.1016/j.scitotenv.2019.04.066.

References

Agarry, S.E., Oguneleye, O.O., Ajani, O.A., 2015. Biosorptive removal of Cadmium (II) ions from aqeous solution by chemically modified onion skin: batch equilibrium, kinetic and thermodynamic studies. Chem. Eng. Commun. 202, 655–673.
Agartan, L., Hayes-Oberst, B., Byles, B.W., Akuzum, B., Pomerantseva, E., Kumbur, E.C., 2019. Influence of operating conditions and cathode parameters on desalination performance of hybrid CDI systems. Desalination 452, 1–8.
Ahmed, M.A., Tewari, S., 2018. Capacitive deionization: processes, materials and state of the technology. J. Electroanal. Chem. 813, 178–192.
AlMarzooqi, F.A., Al Ghaferi, A.A., Saadat, I., Hilal, N., 2014. Application of capacitive deionisation in water desalination: a review. Desalination 342, 3–15.
Anderson, M.A., Cudero, A.L., Palma, J., 2010. Capacitive deionization as an electrochemical means of saving energy and delivering clean water. Comparison to present desalination practices: will it compete? Electrochim. Acta 55, 3845–3856.
Bales, C., Kovalsky, P., Fletcher, J., Waite, T.D., 2019. Low cost desalination of brackish groundwaters by capacitive deionization (CDI) – implications for irrigated agriculture. Desalination 453, 37–53.
Bharath, G., Alhseinat, E., Ponpandian, N., Khan, M.A., Siddiqui, M.R., Ahmed, F., Alsharaeh, E.H., 2017. Development of adsorption and electrosorption techniques for removal of organic and inorganic pollutants from wastewater using novel magnetite/porous graphene-based nanocomposites. Sep. Purif. Technol. 188, 206–218.
Bunce, N.J., Bejan, D., 2011. Mechanism of electrochemical oxidation of ammonia. Electrochim. Acta 56, 8085–8093.
Buragohain, P., Sredeep, S., Saiyouri, N., 2013. A study on the adsorption of ammonium in bentonite and kaolinite. Int. J. Chem. Environ. Biol. Sci. 1 (1), 157–160.
Chakraborty, A., Sun, B., 2014. An adsorption isotherm equation for multi-types adsorption with thermodynamic correctness. Appl. Therm. Eng. 72, 190–199.
Chen, W., Rakhi, R.B., Alshareef, H.N., 2013. Capacitance enhancement of polyaniline coated curved-graphene supercapacitors in a redox-active electrolyte. Nanoscale 5, 4134–4138.
Cheng, C.H., Lehmann, J., Thies, J.E., Burton, S.D., Engelhard, M.H., 2006. Oxidation of black carbon by biotic and abiotic processes. Org. Geochem. 37, 1477–1488.
Chiang, Y.C., Lin, W.H., Chang, Y.C., 2011. The influence of treatment duration on multi-walled carbon nanotubes functionalized by H_2SO_4/HNO_3 oxidation. Appl. Surf. Sci. 257, 2401–2410.
Choi, J.H., Yoon, D.J., 2019. The maximum allowable charge for operating membrane capacitive deionization without electrode reactions. Sep. Purif. Technol. 215, 125–133.
Corapcioglu, M.O., Huang, C.P., 1987. The surface acidity and characterization of some commercial activated carbons. Carbon 25 (4), 569–578.
Elmouwahidi, A., Castelo-Quibén, J., Vivo-Vilches, J.F., Pérez-Cadenas, A.F., Maldonado-Hódar, F.J., Carrasco-Marín, F., 2018. Activated carbons from agricultural waste solvothermally doped with sulphur as electrodes for supercapacitors. Chem. Eng. J. 334, 1835–1841.
Gaikwad, M.S., Balomajumder, C., 2017. Simultaneous electrosorptive removal of chromium(VI) and fluoride ions by capacitive deionization (CDI): multicomponent isotherm modeling and kinetic study. Sep. Purif. Technol. 186, 272–281.
Garland, J.E., Assiongbon, K.A., Pettit, C.M., Emery, S.B., Roy, D., 2002. Kinetic analysis of electrosorption using fast Fourier transform electrochemical impedance spectroscopy: underpotential deposition of Bi^{3+} in the presence of coadsorbing ClO_4^- on gold. Electrochim. Acta 47, 4113–4124.
Golub, D., Oren, Y., Soffer, A., 1987. The electrical double layer of carbon and graphite electrodes: Part IV. dependence of carbon electrode dimensions and electrical capacity on pH. J. Electroanal. Chem. Interfacial Electrochem. 227, 41–53.
Hemmatifar, A., Oyarzun, D.I., Palko, J.W., Hawks, S.A., Stadermann, M., Santiago, J.G., 2017. Equilibria model for pH variations and ion adsorption in capacitive deionization electrodes. Water Res. 122, 387–397.
Huang, C.P., 1976. The electrical double layer of γ-Al_2O_3-electrolyte system. In: Kerker, M. (Ed.), Colloid & Interface Science. vol. VI. Academic Press, Inc., pp. 29–44.
Huang, J., Kankanamge, N.R., Chow, C., Welsh, D.T., Li, T., Teasdale, P.R., 2018. Removing ammonium from water and wastewater using cost-effective adsorbents: a review. J. Environ. Sci. 63, 174–197.
Ioannidou, O., Zabaniotou, A., 2007. Agricultural residues as precursors for activated carbon production—a review. Renew. Sust. Energ. Rev. 11, 1966–2005.
Iskander, S.M., Novak, J.T., He, Z., 2018. Enhancing forward osmosis water recovery from landfill leachate by desalinating brine and recovering ammonia in a microbial desalination cell. Bioresour. Technol. 255, 76–82.
Kapałka, A., Katsaounis, A., Michels, N.L., Leonidova, A., Souentie, S., Comninellis, C., Udert, K.M., 2010a. Ammonia oxidation to nitrogen mediated by electrogenerated active chlorine on Ti/PtO_x-IrO_2. Electr. Commun. 12, 1203–1205.
Kapałka, A., Joss, L., Anglada, Á., Comninellis, C., Udert, K.M., 2010b. Direct and mediated electrochemical oxidation of ammonia on boron-doped diamond electrode. Electr. Commun. 12, 1714–1717.
Karri, R.R., Sahu, J.N., Chimmiri, V., 2018. Critical review of abatement of ammonia from wastewater. J. Mol. Liq. 261, 21–31.

Kim, H., Chung, M.W., Choi, C.H., 2018. NOx-induced deactivation of Pt electrocatalysis towards the ammonia oxidation reaction. Electr. Commun. 94, 31–35.
Li, Y., Stewart, T.C., Tang, H.L., 2018. A comparative study on electrosorptive rates of metal ions in capacitive deionization. J. Water Process Eng. 26, 257–263.
Liu, Y., Liu, Y.J., 2008. Biosorption isotherms, kinetics and thermodynamics. Sep. Purif. Technol. 61, 229–242.
McCafferty, E., 2010. Relationship between the isoelectric point (pH_{pzc}) and the potential of zero charge (E_{pzc}) for passive metals. Electrochim. Acta 55, 1630–1637.
Mia, S., Dijkstra, F.A., Singh, B., 2017. Aging induced changes in biochar's functionality and adsorption behavior for phosphate and ammonium. Environ. Sci. Technol. 51 (15), 8359–8367.
Moradi, O., 2016. Applicability comparison of different models for ammonium ion adsorption by multi-walled carbon nanotube. Arab. J. Chem. 9, S1170–S1176.
Mossad, M., Zou, L., 2013. Evaluation of the salt removal efficiency of capacitive deionisation: kinetics, isotherms and thermodynamics. Chem. Eng. J. 223, 704–713.
Mowla, O., Kennedy, E., Stockenhuber, M., 2019. Mass transfer and kinetic study on BEA zeolite-catalysed oil hydroesterification. Renew. Energy 135, 417–425.
Muttakin, M., Mitra, S., Thu, K., Ito, K., Saha, B.B., 2018. Theoretical framework to evaluate minimum desorption temperature for IUPAC classified adsorption isotherms. Int. J. Heat Mass Transf. 122, 795–805.
Oladunni, J., Zain, J.H., Hai, A., Banat, F., Bharath, G., Alhseinat, E., 2018. A comprehensive review on recently developed carbon based nanocomposites for capacitive deionization: from theory to practice. Sep. Purif. Technol. 207, 291–320.
Ortiz-Bustos, J., Real, S.G., Cruz, M., Santos-Pena, J., 2017. Novel templated mesoporous carbons as electrode for electrochemical capacitors with aqueous neutral electrolytes. Microporous Mesoporous Mater. 242, 221–230.
Pandi, K., Sankar, K.V., Kalpana, D., Lee, Y.S., Selvan, R.K., 2016. Fabrication of solid-state flexible fiber supercapacitor using Agave Americana derived activated carbon and its performance analysis at different conditions. Chem. Sel. 1, 6713–6725.
Park, W., Jang, E., Lee, M.J., Yu, S., Kim, T.H., 2011. Combination of ion exchange system and biological reactors for simultaneous removal of ammonia and organics. J. Environ. Manag. 92, 1148–1153.
Pérez, G., Saiz, J., Ibañez, R., Urtiaga, A.M., Ortiz, I., 2012. Assessment of the formation of inorganic oxidation by-products during the electrocatalytic treatment of ammonium from landfill leachates. Water Res. 46, 2579–2590.
Porada, S., Zhao, R., van der Wal, A., Presser, V., Biesheuvel, P.M., 2013. Review on the science and technology of water desalination by capacitive deionization. Prog. Mater. Sci. 58, 1388–1442.
Ratajczak, P., Suss, M.E., Kaasik, F., Béguin, F., 2019. Carbon electrodes for capacitive technologies. Energy Storage Materials 16, 126–145.
Ribeiro, V.A., de Freitas, I.C., Neto, A.O., Spinace, E.V., Silva, J.C.M., 2017. Platinum nanoparticles supported on nitrogen-doped carbon for ammonia electro-oxidation. Mater. Chem. Phys. 200, 354–360.
Saffarionpour, S., Tam, S.Y.S., Van der Wielen, L.A.M., Brouwer, E., Ottens, M., 2019. Influence of ethanol and temperature on adsorption of flavor-active esters on hydrophobic resins. Sep. Purif. Technol. 210, 219–230.
Sandeep, K.C., Shinde, S.S., Mistry, K., Mohan, S., Bhanja, K., Mandal, D., Mahajani, 2017. Adsorption kinetics on the recovery of hydrogen isotopes from helium using palladium particle bed. Int. J. Hydrog. Energy 42, 29300–29309.
Sharma, K., Mayes, R.T., Kiggans Jr, J.O., Yiacoumi, S., Gabitto, J., DePaoli, D.W., Dai, S., Tsouris, C., 2013. Influence of temperature on the electrosorption of ions from aqueous solutions using mesoporous carbon materials. Sep. Purif. Technol. 116, 206–213.
Shih, Y.J., Su, C.C., Huang, C.P., 2015. The synthesis, characterization, and application of a platinum modified graphite electrode (Pt/G) exemplified by chloride oxidation. Sep. Purif. Technol. 156, 961–971.
Shih, Y.J., Huang, Y.H., Huang, C.P., 2017. Oxidation of ammonia in dilute aqueous solutions over graphite-supported α- and β-lead dioxide electrodes (PbO_2@G). Electrochim. Acta 257 (10), 444–454.
Shih, Y.J., Huang, Y.H., Huang, C.P., 2018. In-situ electrochemical formation of nickel oxyhydroxide (NiOOH) on metallic nickel foam electrode for the direct oxidation of ammonia in aqueous solution. Electrochim. Acta 281, 410–419.
Sing, K.S.W., Everett, D.H., Haul, R.A.W., Moscou, L., Pierotti, R.A., Rouquerol, J., Siemieniewska, T., 1985. Reporting physisorption data for gas/solid systems with special reference to the determination of surface area and porosity. Pure Appl. Chem. 57, 603–619.
Singh, B., Fang, Y., Cowie, B.C.C., Thomsen, L., 2014. NEXAFS and XPS characterisation of carbon functional groups of fresh and aged biochars. Org. Geochem. 77, 1–10.
Stüeken, E.E., Kipp, M.A., Koehler, M.C., Buick, R., 2016. The evolution of Earth's biogeochemical nitrogen cycle. Earth Sci. Rev. 160, 220–239.
Stumm, W., Huang, C.P., Jenkins, S.R., 1970. Specific chemical interaction affecting the stability of dispersed systems. Croat. Chem. Acta 42, 223–244.
Sun, Z., Chai, L., Liu, M., Shu, Y., Li, Q., Wang, Y., Wang, Q., Qiu, D., 2018. Capacitive deionization of chloride ions by activated carbon using a three dimensional electrode reactor. Sep. Purif. Technol. 191, 424–432.
The Council of the European Union, 1998. Council directive 98/83/EC of 3 November 1998 on the quality of water intended for human consumption. Off. J. Eur. Communities (doi:2004R0726 - v.7 of 05.06.2013).
The Council of the European Union, 2000. Directive 2000/60/EC of the European Parliament and of the council of 23 October 2000 establishing a framework for community action in the field of water policy. Official Journal of the European Parliament https://doi.org/10.1039/ap9842100196.
Wang, J., Huang, C.P., Allen, H.E., Cha, D.K., Kim, D.W., 1998. Adsorption characteristics of dye onto sludge particulates. J. Colloid Interface Sci. 208, 518–528.
Wells, N.S., Kappelmeyer, U., Knoller, K., 2018. Anoxic nitrogen cycling in a hydrocarbon and ammonium contaminated aquifer. Water Res. 142, 373–382.
Wimalasiri, Y., Mossad, M., Zou, L., 2015. Thermodynamics and kinetics of adsorption of ammonium ions by graphene laminate electrodes in capacitive deionization. Desalination 357, 178–188.
Wu, T., Wang, G., Zhan, F., Dong, Q., Ren, Q., Wang, J., Qiu, J., 2016. Surface-treated carbon electrodes with modified potential of zero charge for capacitive deionization. Water Res. 93, 30–37.
Xu, K., Lin, W., Wu, J., Peng, J., Xing, Y., Gao, S., Ren, Y., Chen, M., 2015. Construction and electronic properties of carbon nanotube hybrids with conjugated cubic silsesquioxane. New J. Chem. 39, 8405–8415.
Yahya, M.A., Al-Qodah, Z., Ngah, C.W.Z., 2015. Agricultural bio-waste materials as potential sustainable precursors used for activated carbon production: a review. Renew. Sust. Energ. Rev. 46, 218–235.
Yao, H., Li, H., Xu, J., Zuo, L., 2018. Inhibitive effects of chlortetracycline on performance of the nitritation-anaerobic ammonium oxidation (anammox) process and strategies for recovery. J. Environ. Sci. Eng. 70, 29–36.
Zebardast, H.R., Rogak, S., Asselin, E., 2014. Potential of zero charge of glassy carbon at elevated temperatures. J. Electroanal. Chem. 724, 36–42.
Zeng, F., Zhao, Q., Jin, W., Liu, Y., Wang, K., Lee, D.J., 2018. Struvite precipitation from anaerobic sludge supernatant and mixed fresh/stale human urine. Chem. Eng. J. 344, 254–261.
Zhang, C., He, D., Ma, J., Tang, W., Waite, T.D., 2018a. Faradaic reactions in capacitive deionization (CDI) - problems and possibilities: a review. Water Res. 128, 314–330.
Zhang, C., He, D., Ma, J., Waite, D., 2018b. Active chlorine mediated ammonia oxidation revisited: reaction mechanism, kinetic modelling and implications. Water Res. 145, 220–230.
Zhang, M., Li, M., Wang, R., Qian, Y., 2018c. Effects of acute ammonia toxicity on oxidative stress, immune response and apoptosis of juvenile yellow catfish Pelteobagrus fulvidraco and the mitigation of exogenous taurine. Fish Shellfish Immunol. 79, 313–320.
Zhao, Y., Zhang, B., Zhang, X., Wang, J., Liu, J., Chen, R., 2010. Preparation of highly ordered cubic NaA zeolite from halloysite mineral for adsorption of ammonium ions. J. Hazard. Mater. 178, 658–664.
Zornitta, R.L., Ruotolo, L.A.M., 2018. Simultaneous analysis of electrosorption capacity and kinetics for CDI desalination using different electrode configurations. Chem. Eng. J. 332, 33–41.
Zornitta, R.L., Lado, J.J., Anderson, M.A., Ruotolo, L.A.M., 2016. Effect of electrode properties and operational parameters on capacitive deionization using low-cost commercial carbons. Sep. Purif. Technol. 158, 39–52.